J Ther Eng, Vol. 10, No. 4, pp. 1021−1043, July, 2024

Journal of Thermal Engineering
Web page info: https://jten.yildiz.edu.tr
DOI: 10.14744/thermal.0000852

Research Article

Numerical study of flow behavior and heat transfer of ternary water-based nanofluids in the presence of suction/injection, stretching/shrinking sheet

Gul M. SHAIKH[1], Abid A. MEMON[1], M. Asif MEMON[1], Ubaidullah YASHKUN[1], Adebowale Martins OBALALU[2], Hasan KOTEN[3,*]

[1]Department of Basic Sciences and Humanities, Sukkur IBA University, Sukkur, Sindh, 65200, Pakistan
[2]Department of Mathematics, Augustine University Ilara Epe, Lagos, 106103, Nigeria
[3]Department of Mechanical Engineering, Istanbul Medeniyet University, Istanbul, 34700, Türkiye

ARTICLE INFO

Article history
Received: 30 December 2023
Revised: 19 April 2024
Accepted: 26 April 2024

Keywords:
Slip Flow Boundary Conditions; Stagnation Point; Stretching/Shrinking Sheet; Suction/Injection; Ternary Nanofluid

ABSTRACT

Research on ternary hybrid nanofluids is driven by the hope that combining various nanoparticles will lead to better heat transfer efficiency, thermal conductivity, as well as other desired properties. The goal of study is to create a nanofluid that performs better than its binary equivalents by deliberately choosing and combining nanoparticles with different sizes, designs, and thermal conductivities. This research delves into the intricacies of stagnation point flow, taking into account suction/injection, a stretching/shrinking sheet, and slip flow boundary conditions. Employing a ternary hybrid nanofluid (THNF) composed of titanium oxide, silver, and zinc oxide provides insights into the velocity field and thermal characteristics. The study leverages the Tiwari Das nanofluid model and boundary flow equations in two dimensions. The governing equations undergo a transformation into a system of ordinary differential equations (ODEs) via a similarity transformation. These ODEs are subsequently tackled using the finite element method. A meticulous parametric study is executed, manipulating the stretching/shrinking parameter, suction/injection parameter, slip flow parameter, and total volume fraction of the ternary nanofluids. The chosen ranges for these parameters are -1 to 0.5, -1 to 1, 0 to 1, and 0.03 to 0.3, respectively. The observed trend reveals a consistent decrease in the percentage change in temperature concerning the ambient temperature with an increase in normalized distance from the stagnation point, whether the sheet is stretching or shrinking. Notably, the temperature decline is more pronounced in the case of a shrinking sheet. Additionally, in instances involving injection, the transformation from a shrinking sheet to a stretching one exerts a more substantial impact on the percentage change in temperature relative to ambient conditions compared to the suction case. The novelty of the work lies in the study's discovery of correlations for average velocity and average temperature profiles related to the slip flow parameter, suction parameter, and stretching/shrinking parameter, providing a more accurate estimation.

Cite this article as: Shaikh GM, Memon AA, Memon MA, Yashkun U, Obalalu AM, Koten H. Numerical study of flow behavior and heat transfer of ternary water-based nanofluids in the presence of suction/injection, stretching/shrinking sheet. J Ther Eng 2024;10(4):1021−1043.

***Corresponding author.**
*E-mail address: hasan.koten@medeniyet.edu.tr, hkoten@gmail.com

This paper was recommended for publication in revised form by Editor-in-Chief Ahmet Selim Dalkılıç

INTRODUCTION

Observations indicate that when a fluid encounters a solid surface, it splits into two parts and flows through what's known as a "stagnation point." This phenomenon has unique features such as heat transfer, mass deposition rates, and fluid pressure, distinct from other industrial processes occurring at stagnation points. Early studies by [1] and [2] marked the first instances of observing stagnation point flow. Authors like Chiam [3] and Khashi'ie et al. [4] were pioneers in recognizing and studying stagnation point flow, using methods like stretching sheets and deformable plates. Recent technological progress and demand, especially in areas like discs, cylinders, and wedges, have led to increased utilization of these shapes for studying stagnation point flow.

When tiny metallic particles, almost at the nano-scale, are combined with regular fluids such as water, glycols, and oil, they create a potent substance known as nanofluids. These nanofluids show a notable increase in thermal conductivity. Although their thermal conductivity may not surpass that of conventional fluids like water or glycol, limiting their application in scenarios requiring heightened heat transfer, the situation changes when metallic particles are introduced. By blending these particles with standard fluids, nanofluids gain remarkable strength and exhibit significantly improved thermal conductivity. Consequently, they can be confidently employed in various heat transfer applications, consistently delivering positive outcomes.

In a notable experiment by Choi and Eastman [5], it was demonstrated that introducing metallic particles, even in concentrations less than 1% in conventional fluids, could create a material with thermal conductivity nearly double that of the fluids alone. Subsequent research [6] extended this finding, revealing that the addition of nano-sized ceramic and metallic particles to conventional fluids leads to an increase in thermal conductivity, an enhancement not achievable with regular conventional fluids. Additionally, [7] provided insights, explaining that the thermal conductivity of nanofluids is influenced by factors such as particle shape and size, thermophysical properties, aggregation, and the fluid's arrangement over the surface of interest.

Hybrid nanofluids represent an innovative class of fluids formed by combining different types of nanoparticles with a base fluid. These resulting nanofluids exhibit exceptional heat transfer capabilities, drawing significant attention in various industrial applications. Research on their synthesis and manufacturing has been extensively explored and documented in numerous articles [8-13]. Common nanomaterial combinations, such as (Cu, Ag), (Al2O3, CuO, Fe2O3), and carbon-related nanomaterials (MWCNTs, graphite, CNTs), are frequently utilized to enhance heat transfer characteristics, as evidenced by various studies.

To scrutinize the influence of the boundary layer, two key mathematical models—the Buongiorno [14] and Tiwari and Das [15] models—have been extensively employed across numerous articles to delve into the intricacies of nanofluid transport. The Buongiorno model finds common application in scenarios involving flow in stretching domains, as corroborated by several pertinent studies [16-25]. In a specific investigation [26], the power law model was employed on the base fluid, introducing variations in material properties based on the power law index, and utilizing a stretching sheet to delve into the heat transfer characteristics of nanoparticles. Notably, industrial settings predominantly feature the use of materials with Newtonian behavior, warranting focused attention from researchers on materials exhibiting such behavior. A comprehensive study [27] utilized the Tiwari and Das nanofluids model to explore a sheet under suction conditions ranging from 0 to 1.5. Remarkably, the study concluded that, even in the presence of a magnetic effect, the heat transfer rate of the hybrid combination involving alumina and copper in the base fluid surpassed that of copper-water individually. Regarding research gaps, one possible avenue of inquiry would be to delve deeper into the pragmatic consequences of utilizing hybrid nanofluids in actual industrial settings. More concentrated research on the flexibility, economic feasibility, and long-term viability of these hybrid nanofluids in applications in industry could provide a substantial contribution to the current body of knowledge, even though previous investigations have demonstrated their increased heat transfer characteristics.

In certain scenarios, incorporating flow consequences becomes a viable consideration, particularly when the flow exhibits significant relevance. Among these consequences, the suction and injection boundary condition has emerged as a focal point, attracting heightened attention from contemporary researchers. This boundary condition is hailed for its efficacy in regulating energy and external flow in regions dominated by boundary layer flow, achieved through the application of suction and injection conditions. Furthermore, it proves instrumental in averting separation at the boundary. The implementation of this boundary condition necessitates the surface to mimic a porous material or a perforated screen. Moreover, the condition exerts a notable influence on decelerating airflow at the boundaries. The seminal work on the suction and injection condition is documented in article [28], showcasing its potential to comprehensively modify and regulate the flow field. Owing to its consequential impact, unique patterns, and distinct flow characteristics, the suction boundary condition has been scrutinized in various articles [29, 30], exploring diverse surfaces and sheets.

Dealing with a stretching surface is not a common practice because it is associated with numerous applications, including cooling microelectronics, providing manufacturing facilities in tempering iron, deep drawing, polymer extrusion, and rapid jet. This is why it requires technical handling, and many researchers are interested in it. An investigation [31] was conducted to study the movement in the boundary layer for this purpose. Working on this topic

is not only important but also challenging for researchers because it can be influenced by instability in actual mechanics. Recently, researchers and scientists have started showing interest in this topic, particularly in how to deal with unsteady boundary layers. This is because there are many applied designs, such as periodical fluid motion, where dealing with boundary layer movement becomes necessary [32-35].

The study examined by [36] investigated the thermal conductivity of a ternary hybrid nanofluid containing ethylene glycol, water, titania-zinc oxide, and Multi-walled Carbon Nanotubes (MWCNTs). The experiment showed that thermal conductivity of ternary hybrid nanofluids had a beneficial impact by temperature increases and MWCNT concentration. At T = 50°C and 0.4% MWCNTs, the maximum boost of 17.82% was seen. When juxtaposed with data from experiments, a suggested mathematical model showed excellent precision. Although this research concentrated on the ternary hybrid nanofluid, a more thorough understanding of the ways in which individual nanoparticles improved thermal conductivity may have been necessary to help researchers customize nanofluids for particular purposes.

The experimental investigation [37] examined the dynamic viscosity and thermal conductivity of Cu-SiO2-MWCNT/water ternary hybrid nanofluid (THNF) over a temperature that ranged from 15 °C to 65 °C and a volume range of concentrations of 1% to 3%. In comparison to single and binary nanofluids, the inventive usage of metal, oxides of metal, and ternary polymer nanoparticles in the nanofluid manufacturing procedure showed higher temperature conductivity and dynamic viscosity. The viscosity and thermal conductivity computational models that were suggested showed excellent reliability, with R-square values above 99% and lowest error rates of 1.167% and 1.327%, respectively. Examining the equilibrium and long-term behavior of ternary hybrid nanofluids in various circumstances could have been a worthwhile endeavor. These knowledge gaps pointed to areas that further research could address to improve for comprehension of ternary hybrid nanofluids and possible usage.

An experimental study [38] was conducted to investigate forced convection with heat transfer by introducing three doped magnetic nanoparticles into a circular tube. The ternary nanofluid was composed of zinc oxide, MWCNT, and manganese ferrite to form new nanomaterials. The experimental results demonstrated that increasing the nanoparticle concentration enhances thermal conductivity, incorporating the magnetic field improves convection in the channel. It was also observed that using a Reynolds number of 2200 with 0.2 volume concentration of nanomaterials and 400 G of magnetic field resulted in the maximum improvement in the Nusselt number. Furthermore, there might be a research vacuum in figuring out the best circumstances and dosages to maximize the improvement in the conductivity of heat and Nusselt value. The study conducted by [39] focused solely on a contracting sheet for studying the flow of ternary hybrid nanofluids in the presence of electrical forces. The research highlighted that examining heat transfer along the sheet provides unparalleled insights, and analyzing the impact of nanomaterial shapes revealed that the shape factor had a negligible effect on the heat transfer rate. The work [40] created a mathematical framework that included dependent on temperature viscous and Casson hybrid nanofluid for layered non-miscible liquid flow in a sloped channel with pulsatile pressure gradient. It provided knowledge about fluid behavior and heat transfer rates by analyzing the impact of various parameters on temperature, concentration, velocity, and shear stress.

In the realm of industrial and manufacturing applications, addressing slip effects within the boundary condition becomes imperative. Various scenarios, such as flow across greased surfaces, surface roughness, encased flow material, and striated sheets [41], require a nuanced consideration of slip effects. This boundary condition is extensively employed in commercial processes, notably for controlling the flow field in reactors and combined surfaces [42]. Discussions about slip effects often involve the imposition of linear slip velocity [43], with studies [44] and [45] making significant contributions through theoretical assessments and the incorporation of no-slip boundaries in the context of fluid flow at the stagnation point. These studies underscore that augmenting slip effects correlates with an enhanced heat transfer rate. A model of Casson nanofluids was employed by Paul et al. [46] to investigate the impact of an electromagnetic field on heat transfer through a three-dimensional rotatory disc, alongside an analysis of the influence of Darcy-Forchheimer effects. The study revealed that compared to Casson nanofluids, heat and mass transpiration increased by 19.23% and 51.28% respectively. Additionally, it was concluded that implementing Casson nanofluids led to an 8.9% decrease in skin friction. To assess the impact of Casson nanofluids, Paul et al. [47] examined a rotatory disk using transformer oil, considering incompressible fluids and magnetic fields. They observed 10.93% and 8.86% increases in heat and mass transfer, respectively, with the Casson nanofluids model. Successful implementation of the Casson nanofluids model led to a significant decrease in skin friction, enhancing heat transfer. Utilizing the Casson nanofluids model in conjunction with the Darcy-Forchheimer condition, researchers Paul et al. [48] investigated the passage of ternary hybrid nanofluids through a porous stretching circular cylinder to elucidate heat transfer characteristics. Through rigorous numerical simulations, it was discerned that skin friction exhibited an 11% increase in the case of hybrid nanofluids, surpassing that observed with traditional nanofluids. For a more in-depth exploration of fluid flow and heat transfer under slip effects, additional references [49-53] provide valuable insights.

After a meticulous review of the significance of nanofluids, suction, stretching, and fluid flow at the stagnation

point, it becomes evident that delving into such fluid flow phenomena is imperative and widely applied in various industrial and manufacturing contexts. Therefore, this article aims to investigate ternary-based hybrid nanofluids at the stagnation point, comprising silver, titanium oxide, and zinc oxide in equal volume fractions in the base fluid of water on a stretching/shrinking sheet. We will consider a linear slip boundary condition at the stretching/shrinking surface, including suction boundary conditions. Additionally, we will assume that the ambient velocity varies linearly. The article will conduct parametric studies on the volume fraction of ternary nanofluids, the stretching/shrinking parameter, the slip flow parameter, and the suction/injection parameter. To observe the fluid flow phenomenon and heat transfer, we will solve the partial differential equations of the boundary layer, as used in the studies on Tiwari and Das nanofluids, utilizing the finite element package COMSOL 6.0. Furthermore, we will consider a specific case to elucidate the heat transfer phenomenon by imposing particular temperatures along the moving boundary and ambient temperature. The validity of the results will be assessed through a mesh-independent test, verification of the governing ordinary differential equations transformed via similarity transformation, and comparison with previous literature. The numerical results will encompass descriptions of the velocity profile, temperature profile, temperature percentage change due to ambient temperature, and the Nusselt number while altering the selected parametric study.

PROBLEM FORMULATION

In the current study, we are going to observe the characteristics and behavior of the ternary hybrid nanofluid at the stagnation points by considering a set of equations for boundary layer flow. These equations are well-known for observing the Tiwari and Das nanofluids [15]. To observe this, let us see the pictorial representation of the passage of ternary nanofluids at the stagnation point at x, y=0 and y>0 in Figure 1. The fluid is set along the stretching and shrinking sheet at the position x=0. Let $U_w(x) = ax$ be the velocity of the stretching and shrinking at the wall, and let $U_\infty(x) = bx$ be the velocity of the fluid in the domain known as the ambient fluid velocity, where a and b are constants. If the sheet is facing the stretching condition, then $a > 0$; if it is shrinking, then $a < 0$. A suction and injection are also applied at the lower boundary of the channel, given with the velocity v_w, as shown in Figure 1.

The fluid that is being studied for its characteristics of forced convection and dynamics is a ternary hybrid nanofluid composed of water as the base fluid and three nanoparticles: zinc oxide, copper, and titanium oxide. To examine the characteristics of temperature distribution, we assume that these nanoparticles are present in the water in equal volume fractions in the base fluid. The thermophysical properties that are altered when these nanoparticles are mixed in the base fluid are calculated and provided in Table 1. Table 1 also describes the thermophysical properties used for the constituents in the mixture. Moreover, we are observing the passage of water-based ternary nanofluid, which is claimed to be more powerful in terms of increasing heat transfer rate compared to mono and hybrid nanofluids. The model of the nanofluids used to investigate fluid flow and heat transfer via stretching and shrinking sheets has been applied in several research articles [49-56] to explore the well-known phenomenon of forced convection problems. The model is straightforward to implement, initially calculating the thermophysical properties of the nanomaterials and combining them with the base fluids to form ternary hybrid nanofluids. [54-60]

Let $w=< w_1, w_2 >$ be the velocity of the fluid along the stretching and shrinking sheet, where suction and slip flow conditions are also imposed. We are observing the passage of nanofluid along the shrinking and stretching sheet, and for this purpose, we are applying the Tiwari and Das nanofluids and boundary layer flow equations to implement this model. The given equations are as follows:

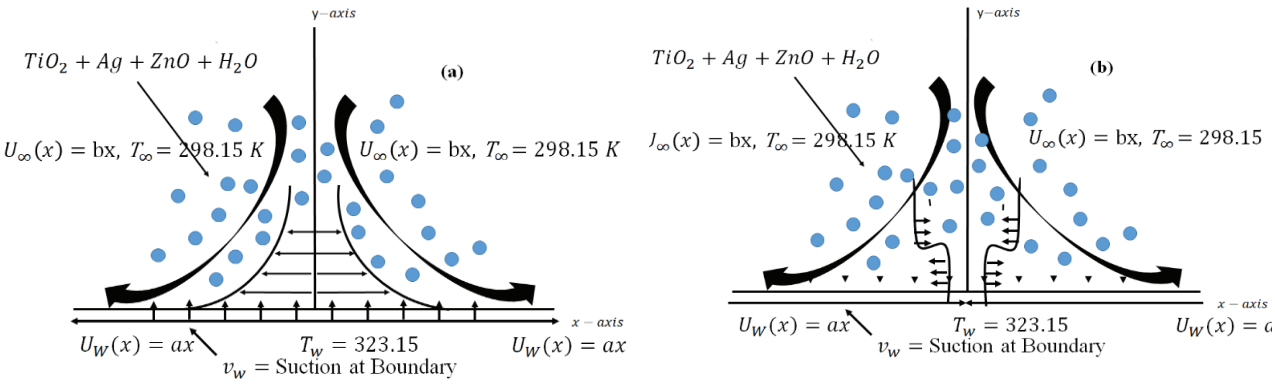

Figure 1. A pictorial representation of stagnation point flow at horizontal sheets under the influence of ternary nanofluid and the boundary conditions (a) stretching sheet (b) shrining sheet.

Table 1. Thermal and physical properties of ternary hybrid nanofluids [54-60]

Symbols	Values or expressions	Descriptions
ϕ_1	ϕ_3	volume fraction of Titanium oxide
ϕ_2	ϕ_3	Volume fraction of Silver
ϕ_3	ϕ_3	Volume fraction of Zinc oxide
ρ_1	4250 [kg/m^3]	Density of Titanium oxide
ρ_2	10500 [kg/m^3]	Density of Silver
ρ_3	5600 [kg/m^3]	Density of Zinc oxide
ρ_{np}	$\frac{\phi_1\rho_1+\phi_2\rho_2+\phi_3\rho_3}{\phi_1+\phi_2+\phi_3}$	Total density of nanoparticles mixture in the base fluid
$(c_p)_1$	686.2 [J/(kg K)]	Specific heat of Titanium oxide
$(c_p)_2$	235 [J/(kg K)]	Specific heat of silver
$(c_p)_3$	495.2 [J/(kg K)]	Specific heat Zinc oxide
$(c_p)_{np}$	$\frac{\phi_1\rho_1(cp)_1+\phi_2\rho_2(cp)_2+\phi_3\rho_3(cp)_3}{\phi\rho_{np}}$	Specific heat of mixture of nanoparticles
ϕ	ϕ_3=0.03, 0.08, 0.16, 0.3	Total volume fraction in the base fluid
κ_1	8.952 [W/(m K)]	Thermal conductivity of TiO
κ_2	429 [W/(m K)]	Thermal cond. of Ag
κ_3	13 [W/(m K)]	Thermal cond. of ZnO
κ_{np}	$\frac{\phi_1\kappa_1+\phi_2\kappa_2+\phi_3\kappa_3}{\phi}$	Total thermal conductivity of nanoparticles
ρ_{bf}	998 [kg/m^3]	Density of base fluid
ρ_{hnf}	$\rho_{bf}(1-\phi)+\phi\rho_{np}$	Density of nanofluid
$(c_p)_{bf}$	4182 [J/(kg*K)]	Specific heat of base fluid
$(c_p)_{hnf}$	$\frac{\rho_{bf}(1-\phi)(c_p)_{bf}+\rho_{np}(1-\phi)(c_p)_{np}}{\rho_{hnf}}$	Specific heat capacity of nanofluid
κ_{bf}	0.597 [W/(m K)]	Thermal conductivity of the base fluid
κ_{hnf}	$\kappa_{bf}\frac{\kappa_{np}+2\kappa_{bf}+2(\kappa_{np}-\kappa_{bf})\phi}{\kappa_{np}+2\kappa_{bf}-(\kappa_{np}-\kappa_{bf})\phi}$	Thermal conductivity of the nanofluids
μ_{bf}	0.000998 [Pa s]	Viscosity of the base fluid
μ_{hnf}	$\frac{\mu_{bf}}{(1-\phi)^{2.5}}$	Viscosity of nanofluid
T_w	323.15 K	Inlet temperature
T_∞	293.15 K	Hot tem
α_{hnf}	$\frac{\kappa_{hnf}}{\rho_{hnf}(c_p)_{hnf}}$	Thermal diffusivity

$$\frac{\partial w_1}{\partial x}+\frac{\partial w_2}{\partial y}=0 \tag{1}$$

$$w_1\frac{\partial w_1}{\partial x}+w_2\frac{\partial w_1}{\partial y}=U_\infty\frac{dU_\infty}{dx}+\frac{\mu_{nf}}{\rho_{nf}}\frac{\partial^2 w_1}{\partial y^2} \tag{2}$$

$$w_1\frac{\partial T}{\partial x}+w_2\frac{\partial T}{\partial y}=\frac{\kappa_{nf}}{\rho_{nf}cp_{nf}}\frac{\partial^2 T}{\partial y^2} \tag{3}$$

We are searching for the numerical solution of equations (1) to (3) subject to the boundary conditions (4) and (5). To accomplish this, we will utilize the built-in software Comsol Multiphysics 6.0, which employs the robust technique of the finite element method. The following boundary conditions are provided to observe the flow [61]:

$$u_1 = U_w(x) + L(\frac{\partial u_1}{\partial y}),\ v_1 = v_w \text{ and } T = T_w \text{ at y=0} \quad (4)$$

$$u_1 = U_\infty(x),\ T = T_\infty \text{ when } y \to \infty \quad (5)$$

Advantages of Boundary Conditions: Applying slip flow boundary conditions along the surface will definitely reduce friction, consequently minimizing the resistance of flow along the surface. It also diminishes the resistance contact during fluid-surface interaction, ultimately enhancing heat transfer from the surface to the fluid. Boundaries that are stretched or shrunk may cause fluid components to deform and stretch, thereby improving mixing. This is particularly advantageous for processes such as chemical reactions and small-scale pumping systems. Additionally, suction, by decreasing the thickness of the boundary layer, can reduce the drag force acting on an object submerged in the fluid.

Initial the governing partial differential equations of Tiwari and Das nanofluid will be transformed into governing odes with the help of similarity transformation given in (6).

$$\eta = (b/\nu_{nf})^{1/2}\,\mathrm{y},\ \psi = (\mathrm{b}\nu_{nf})^{1/2} x f(\eta),\ \theta = \frac{T - T_\infty}{T_w - T_\infty} \quad (6)$$

Where η a normalized similarity variable, v_{nf} is is kinematic viscosity of the tri-hybrid nanofluid. Also, $w_1 = \frac{\partial \psi}{\partial y}$ and $w_2 = -\frac{\partial \psi}{\partial x}$ T is the original temeperature and θ is known as the non-dimensional temperature profile.

The similarity transformation (6) will lead to obtaining the governing ordinary differential equations (ODEs) given in (7) and (8) [61]. These governing ODEs, transformed from the similarity transformation, will be solved using the mathematical interface of Comsol Multiphysics 6.0.

$$\frac{1}{(1-\phi)^{2.5}(1-\phi+\phi\rho_{np}/\phi\rho_{nf})} f''' + ff'' - (f')^2 + 1 = 0 \quad (7)$$

$$\frac{(\kappa_{nf}/\kappa_{bf})}{\Pr(1-\phi+\phi(\rho cp)_{np}/\phi(\rho cp)_{nf})}\theta'' + f\theta' = 0 \quad (8)$$

By considering the transformation (6) and applying it to equations (1) to (3), along with implementing it in boundary conditions (4) and (5), we obtain the governing ODEs (7) and (8) subject to the boundary conditions (9) and (10). Here, λ represents the stretching/shrinking parameter, where a negative value indicates shrinking and a positive value indicates stretching. γ represents the suction/injection parameter, and it is positive for suction. δ represents the slip flow parameter, which is considered positive.

For the current study, we aim to observe the patterns of the variables of interest. To achieve this, we will test various values of these parameters as provided in Table 2. By altering these parameter values, we will analyze the velocity field, temperature profile, and Nusselt number.

$$f'(0) = \lambda + \delta f''(0),\ f(0) = \gamma \text{ and } \theta(0) = 1 \quad (9)$$

$$f'(\eta) \to 1,\ \theta(\eta) \to 0 \text{ as } \eta \to \infty \quad (10)$$

We are using a numerical procedure to solve this problem because the current partial differential equation is a nonlinear equation. Therefore, direct and analytical solutions are not readily available. Here, we are using the finite element-based software Comsol Multiphysics 6.0 to obtain a numerical solution. We utilize the mathematics interface of this software, where we can easily convert equations (7) and (8) into a system of ordinary differential equations (ODEs). Then, we can use the constituent coefficient form of the PDEs within the mathematics interface, which is a built-in tool for solving systems of ODEs.

Suppose that we are using the variable $f' = g$ and $f'' = h$ to convert equations (7) and (8), and as a result, these equations are reduced to a system of ODEs.

$$f' - g = 0 \quad (11)$$

$$f'' - h = 0 \quad (12)$$

Table 2. Parameters of suction/injection, stretching/shrinking, slip flow parameters and others

λ	-1, -0.5, -0.3, 0, 0.3, 0.5	stretching and shrinking parameter
γ	-1, -0.5, -0.3, 0, 0.3, 0.5, 1	Suction/injection
δ	0, 0.4, 0.8, 1	Slip flow parameter
α	$\frac{1}{(1-\phi)^{2.5}(1-\phi+\phi\rho_{np}/\rho_{bf})}$	Leading coefficient of equation (7)
β	$\frac{(\kappa_{nf}/\kappa_{bf})}{\Pr(1-\phi+\phi(\rho c_p)_{np}/(\rho c_p)_{np})}$	Leading coefficient of equation (8)

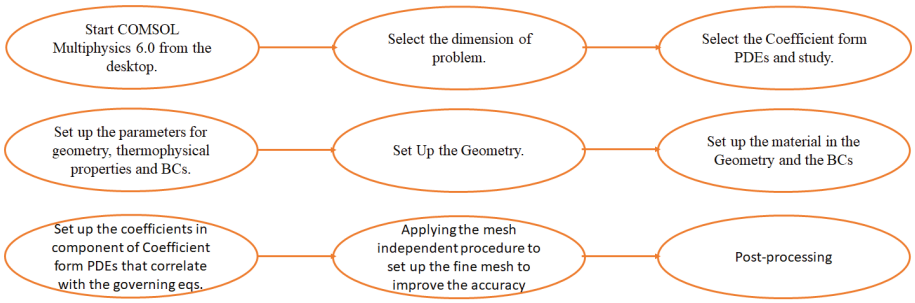

Figure 2. Flow chart of COMSOL working.

$$\frac{1}{(1-\phi)^{2.5}(1-\phi+\phi\rho_{np}/\phi\rho_{nf})}\mathrm{h}'+fh-(\mathrm{g})^2+1=0 \tag{13}$$

$$\frac{(\kappa_{nf}/\kappa_{bf})}{\Pr(1-\phi+\phi(\rho cp)_{np}/\phi(\rho cp)_{nf})}\theta''+f\theta'=0 \tag{14}$$

Also, after the supposition, the boundary conditions will be reduced to:

$$\mathrm{g}(0)=\lambda+\delta h(0),\ f(0)=\gamma \text{ and } \theta(0)=1 \tag{15}$$

$$\mathrm{g}(\eta)\to 1,\ \theta(\eta)\to 0 \text{ as } \eta\to\infty \tag{16}$$

The system can be easily implemented on the mathematics interface of Comsol Multiphysics. It should be noted that we have only converted equation (9) into a system of first-order ODEs because it involved a third derivative. The mathematics interface can handle up to second-order derivatives in the coefficient form of PDEs. Additionally, it is necessary for the boundary conditions to be Dirichlet boundary conditions. The equations (13)-(16) will be systematically solved using the commercial software COMSOL Multiphysics 6.0, as illustrated in the flowchart Figure 2.

Mesh Independent Study and Verification

This is the beauty of almost every numerical approach, whether it involves ODEs or PDEs, used to obtain a numerical solution. They divide the domain of interest into several parts and then obtain solutions one by one for each part to achieve a solution for the entire domain. The procedure of decomposing the whole domain into parts is referred to as the meshing or grid procedure. It is said that the higher the mesh density (i.e., the more elements there are), the higher the accuracy level of the numerical procedure. Obtaining a numerical solution for any governing system is no longer a difficult task. The real challenge lies in ensuring its accuracy, which is accomplished by performing mesh independent tests or grid independence tests. According to the procedure, a single variable is chosen, and by increasing the number of elements, the solution for that

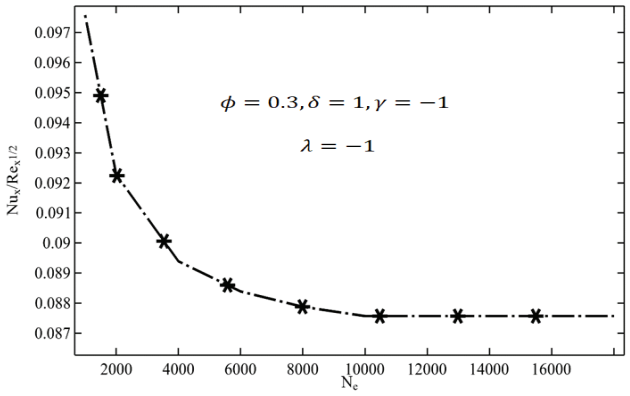

Figure 3. The mesh independent or grid independence test to ensure the accuracy level of the numerical procedure.

variable is obtained. In this process, the difference between the previous and the next solutions is calculated. Once this difference becomes negligible, it is assumed that the numerical solution has achieved mesh independence, and further solutions beyond this point will have errors that are almost negligible. In Figure 3, we have applied this numerical approach, which is based on the finite element method, to obtain a solution for the governing ODEs, and we have determined the variable of interest, which is the Nusselt number. We can observe that as we increase the number of elements from 1000 to 14000, the computation error is reducing. In Figure 3, we can see that the numerical solution has achieved mesh independence when the number of elements exceeds 10,000.

Finally, we have attached Table 3 for verification, which shows that the governing ODEs obtained through a similarity transformation have been satisfied at different parameter values. You can see that there are negligible errors, and we have not come across this type of verification in any article so far, or it may be beyond our current knowledge. However, this verification is demonstrating that the present finite element simulation is a reliable method or code through which phenomena such as fluid flow at the stagnation point under the presence of a stretching/shrinking

Table 3. The verification table for some values of the selected parameter for the ODEs that are transformed from similarity transformation

γ	λ	ϕ	δ	$af''' + ff'' - (f')^2 + 1 = 0$	$b\theta'' + f\theta' = 0$
0	-1	0.3	1	4.98E-16	6.81E-11
0	-0.5	0.3	1	3.30E-16	-2.23E-09
0	-0.3	0.3	1	2.54E-16	3.17E-11
0	0	0.3	1	1.62E-16	-6.22E-11
0	0.3	0.3	1	5.18E-17	-1.75E-07
0	0.5	0.3	1	6.12E-17	-1.58E-12
0.5	-1	0.3	1	2.78E-16	-7.49E-13
0.5	-0.5	0.3	1	1.58E-16	4.14E-09
0.5	-0.3	0.3	1	1.21E-16	4.89E-09
0.5	0	0.3	1	7.82E-17	-1.55E-08
0.5	0.3	0.3	1	4.64E-17	-3.91E-14
0.5	0.5	0.3	1	3.00E-17	-3.91E-12
1	-1	0.3	1	1.24E-16	-1.27E-13
1	-0.5	0.3	1	6.85E-17	-4.38E-15
1	-0.3	0.3	1	5.77E-17	2.72E-15
1	0	0.3	1	3.65E-17	3.24E-15
1	0.3	0.3	1	2.06E-17	-2.28E-12
1	0.5	0.3	1	1.42E-17	-5.49E-11

Table 4. Convergence table for the top 10 values of the parameter to display the convergence in the last iteration

γ	λ	δ	ϕ	Convergence in the last iteration
1	-1	1	0.08	1.3e-09
1	-1	1	0.1	1.5e-08
1	-0.5	1	0.01	7.5e-11
1	-0.5	1	0.04	4.8e-10
1	-0.5	1	0.08	1.1e-10
1	-0.5	1	0.1	1e-08
1	-0.3	1	0.01	8.2e-11
1	-0.3	1	0.04	3.6e-10
1	-0.3	1	0.08	1.1e-10
1	-0.3	1	0.1	6.7e-09

sheet can be accurately observed. Utilizing 7 values for both γ and λ, and 4 values for each of δ and ϕ, this article conducts a total of 784 numerical simulations. Employing a convergence criterion of e-10, we observe convergence in the final step of each numerical solution. While data for all convergences is available, Table 4 will specifically present the convergence results for 10 numerical solutions.

Finally, to enhance reliability, we are comparing our present work with previous numerical work [60]. Our work is more advanced compared to the previous work because we have used our present code to observe the transport and convection qualities of ternary nanofluids, whereas the previous work was limited to mono nanofluids. However, for the purpose of comparison, we have made slight changes to the parameters in our present investigation. In literature, it can be observed that our present numerical code based on the finite element method is comparable to the previous numerical work [61]. We are referring to it for slight verification. Additionally, we can also see that the temperature profile, $\theta(\eta)$, in this figure can be compared to patterns in various articles involving stretching or shrinking sheets with the transportation of nanofluids.

RESULTS AND DISCUSSION

Pattern of Velocity Profile Against the Parameters

In Figure 4(a-d), we endeavored to analyze the velocity profile pattern concerning η. Throughout this analysis, we maintained fixed λ values for each graph. As we progressed from Figure 4(a) to Figure 4(d), we altered the suction parameter γ. In Figure 4(a), it is evident that for each fixed value of λ, δ, ϕ, and γ, the velocity of nanofluids increases with rising values of η. Additionally, in Figure 4(a), it is observable that when λ values increase, the velocity also increases. Here, γ has a value of -1, signifying the injection case, and the δ value is 1, indicating a slip flow condition imposed in this domain. Nevertheless, the velocity profile consistently increases against the values of η, whether due to sheet stretching or shrinking. Similarly, upon analyzing Figure 4(b) to Figure 4(d), we noted that increasing

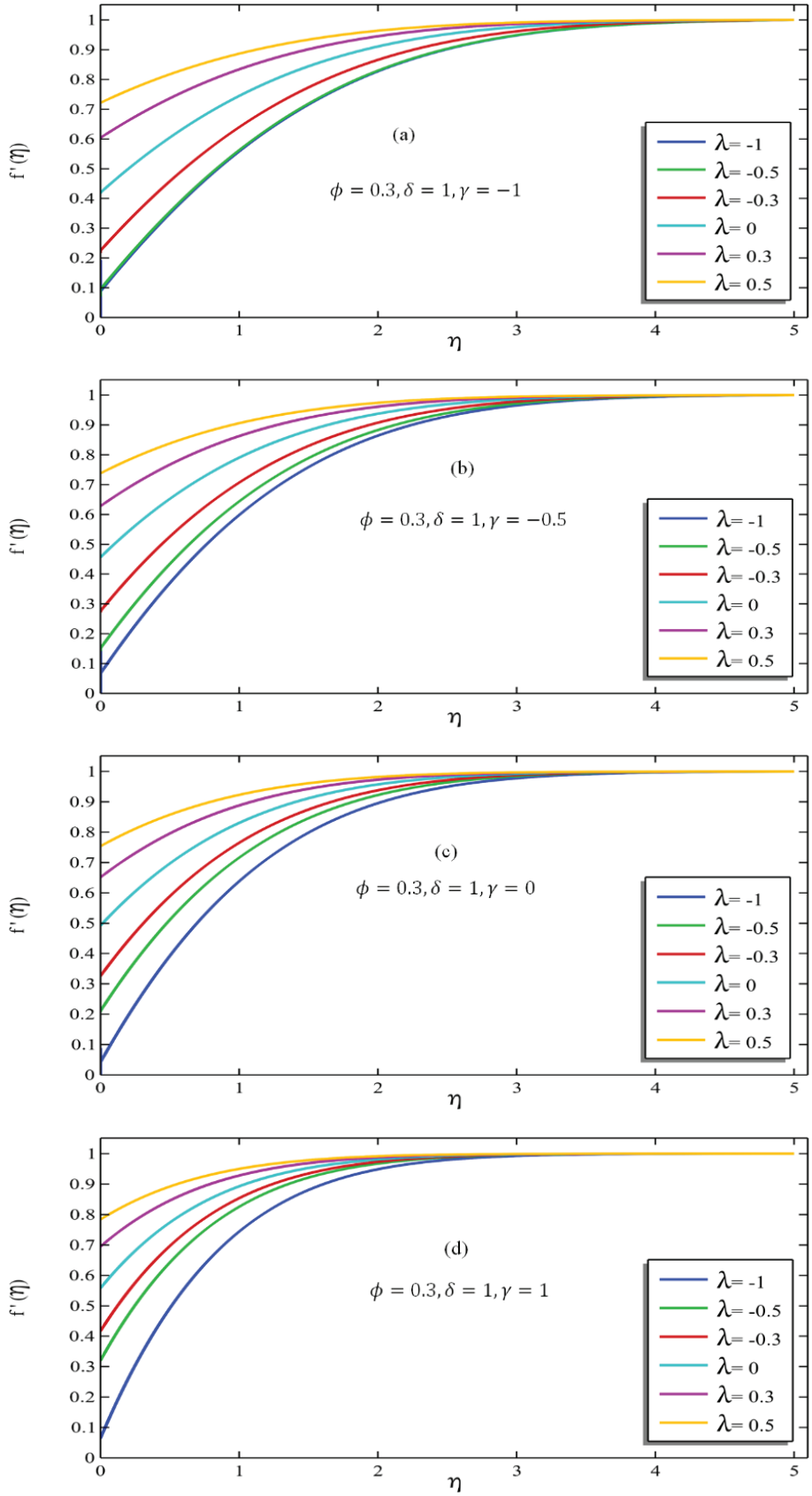

Figure 4. (a-d) Velocity profile vs η with the impact of λ values and suction/injection parameters with fixed volume fraction and slip flow parameter.

λ values do not significantly impact the velocity of nanofluids. In these three figures, where the suction parameter ranges from -0.5 to 0.5, Figure 4(c) is notable. Even in the absence of suction or injection, increasing λ values do not influence the velocity profile pattern. Instead, an increment in λ values cause an overall increase in the velocity profile. In Figure 4(d), where γ is 0.5, there is also no significant impact observed on the velocity profile due to γ values.

In Figure 5(a-c), we are re-examining the velocity profile, with fixed volume fraction and slip flow parameters. These graphs are specifically designed to determine the velocity profile pattern with increasing values of the slip flow parameter. In Figure 5(a), despite fixed parameters, the velocity profile gradually upgrades against η. As the slip flow parameter increases in Figure 5(a), the velocity profile gradually declines. In this case, λ has a value of -1, indicating a shrinking case. Moving on to Figure 5(b), where $\lambda = 0$, representing a stationary sheet, increasing the slip flow parameter, δ, leads to an increase in the velocity profile. This implies that the sheet's movement significantly impacts the velocity profile due to altering values of δ. Now, considering Figure 5(c), with fixed λ values at 0.5 for all graphs, increasing δ values support the velocity profile, indicating a stretching sheet. In Figure 5(c), there is a noticeable increase in the velocity increment for each δ value increment in the case of a stationary or stretching sheet.

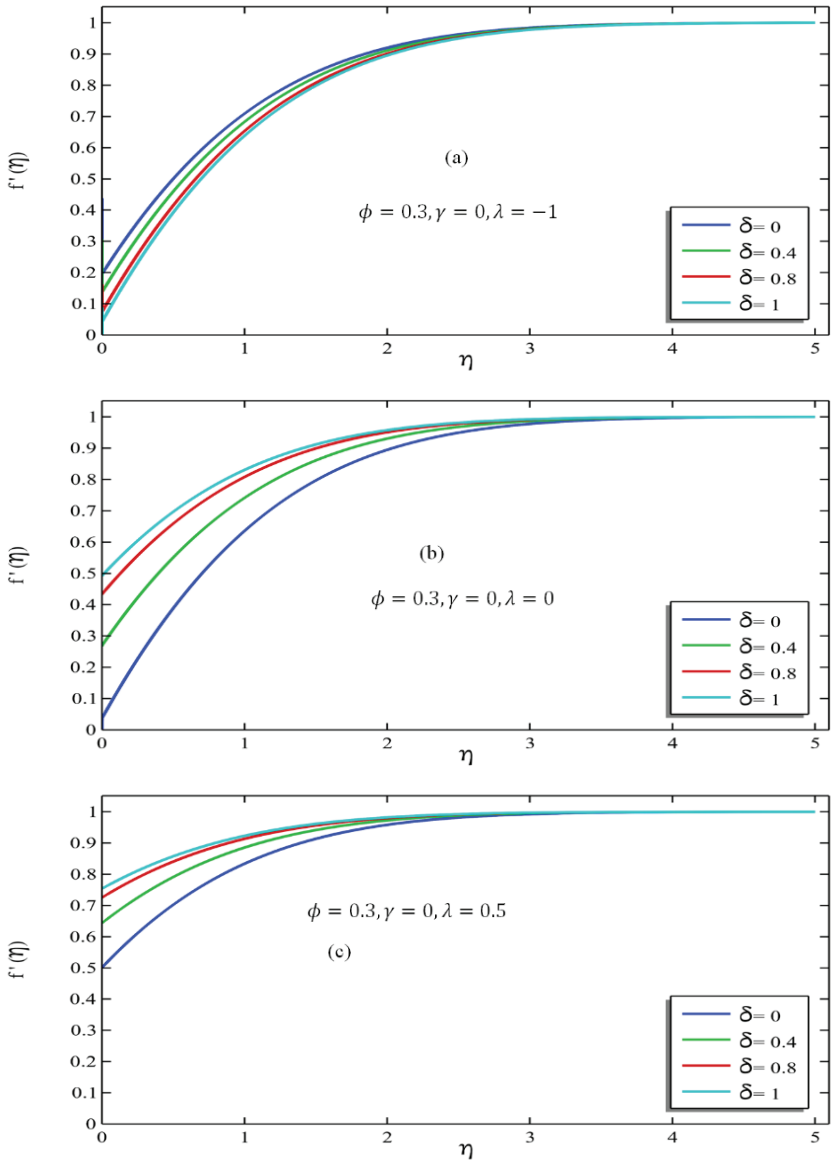

Figure 5. (a-c) Velocity profile vs η with the impact of δ values and stretching/shriniking parameter with fixed suction/injection and volume fraction of nanofluids.

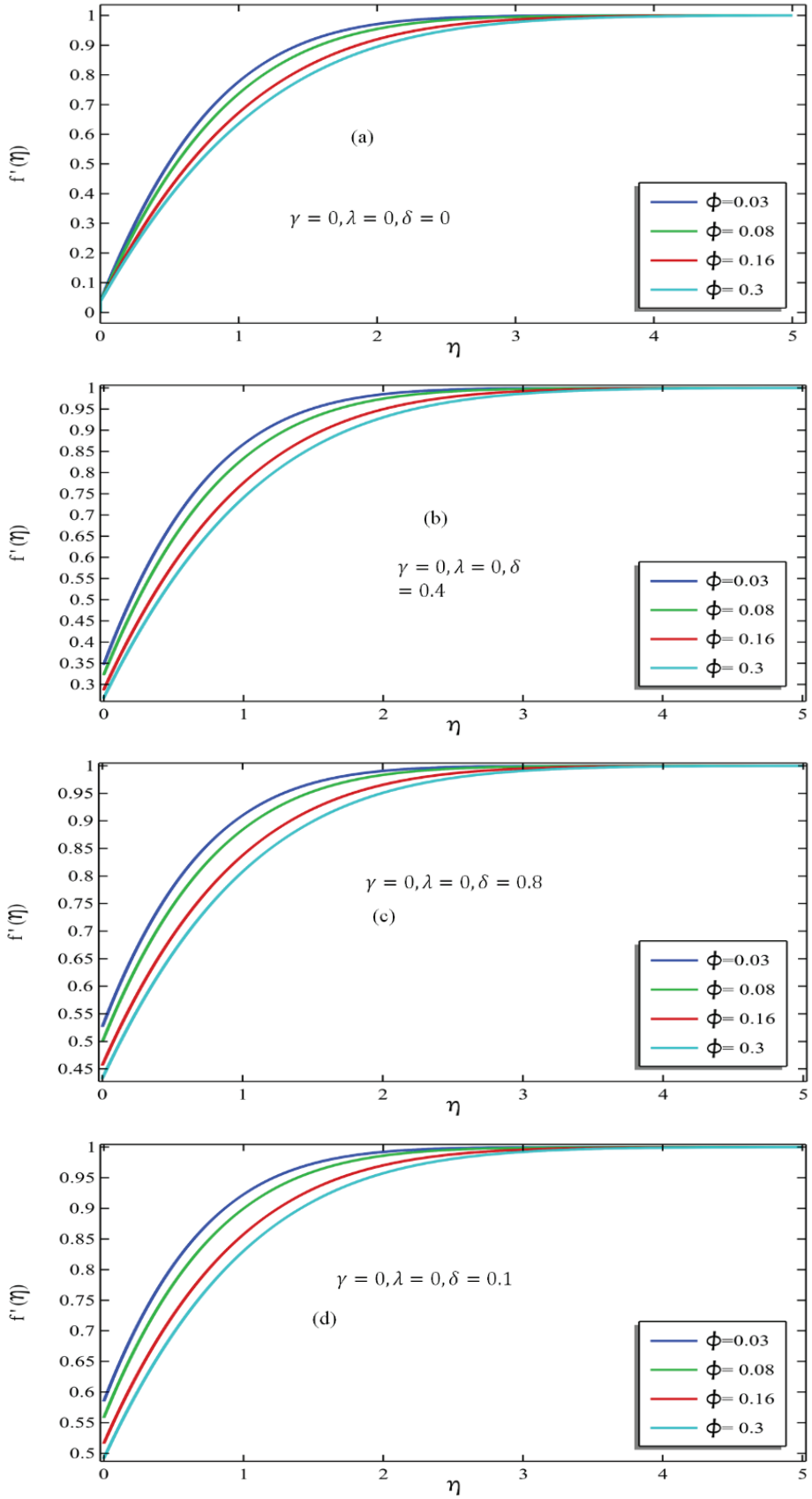

Figure 6. (a-c) Velocity profile vs η for all the values of volume fraction and the slip flow parameter with fixed λ and γ values.

In Figure 6(a-c), we are examining the pattern of the velocity profile against an increasing value of the volume fraction. Here, we have fixed the γ and λ values and gradually increased the slip flow parameter to observe if there is any impact on the pattern of the velocity profile with increasing ϕ. In Figure 6(a), it can be observed that if we fix all parameters except the volume fraction, increasing the volume fraction leads to a decrease in the velocity profile. This is likely due to the increasing density of ternary hybrid nanofluids, resulting in a decrease in the velocity profile with an increase in the volume fraction. Similarly, in Figure 6(b), it is observed that increasing the slip flow parameter while trying to check the pattern of the velocity profile leads to a decrease in the velocity profile, despite the attempt to increase it. Likewise, in Figure 6(c) and Figure 6(d), we observe the same pattern where the volume fraction of ternary hybrid nanofluids does not support an increment in velocity, even when we increase the slip velocity. This can be clearly seen when we compare the minimum velocity at η=0 in Figure 6(a) and Figure 6(d). Additionally, we have already observed this impact in Figure 5(a-d). The same patterns of velocity vs. η can be determined in several articles [62-64].

Physical mechanism

The augmentation of suction parameters enhances fluid influx due to an increased suction effect. Concurrently, heightened slip flow parameters on the sheet contribute to a reduced drag coefficient, consequently causing a decline in both the velocity profile and drag. Nevertheless, for a stationary sheet, intensified slip effects enhance the drag, resulting in an augmented velocity profile. Lastly, the escalation of volume fraction is notably associated with an increase in the density of ternary hybrid nanofluids, inducing a subsequent reduction in fluid velocity.

Finally, a regression equation is calculated using the online calculator [65]. Equation (17) is provided below, and accompanying this, Table 5 displays the top 20 best parameter estimation for minimum absolute errors. These errors are calculated by taking the difference between the exact value of average velocity $f'(\eta)_{avg}$ and the value $f'^{\wedge}(\eta)_{avg}$ calculated from the regression equation derived in equation (17). According to the given Table 5, it can be understood that using γ = -0.3, λ = -0.3, δ = 0.8 and ϕ_3 = 0.04 the equation (17) can be used as the best estimator for the average velocity along the stretching/shrinking sheet.

$$\hat{f'}(\eta)_{avg} = 0.910641 + 0.0354591\,\gamma + 0.076496\,\lambda + 0.0447607\delta - 0.478292\phi_3 \quad (17)$$

Table 5. Top 20 values of the parameters that yield the minimum absolute error when the exact average velocity along the line compared to the estimated average velocity due to regression equation

γ	λ	δ	ϕ_3	$f'(\eta)_{avg}$	$\hat{f'}(\eta)_{avg}$	$\lvert f'(\eta)_{avg} - \hat{f'}(\eta)_{avg} \rvert$
-0.3	-0.3	0.8	0.04	0.89378	0.893731	4.86E-05
-1	0	1	0.01	0.91509	0.91516	6.97E-05
0	0.3	0.4	0.01	0.9468	0.946711	8.88E-05
0.3	0.3	0.8	0.04	0.96121	0.960904	0.000306
0.5	0.5	0.4	0.04	0.96505	0.965391	0.000341
-1	0	0.8	0.08	0.87307	0.872727	0.000343
0.5	0	1	0.04	0.95438	0.954	0.00038
-0.3	-0.3	0.8	0.01	0.90847	0.90808	0.00039
-0.3	0.5	0.8	0.01	0.96968	0.969277	0.000403
0.3	0	0.8	0.01	0.95187	0.952304	0.000434
0.5	0.3	0.4	0.04	0.94963	0.950092	0.000462
0.3	-0.3	0.8	0.08	0.89638	0.895875	0.000505
0	0	1	0.01	0.95113	0.950619	0.000511
-0.5	0.5	1	0.01	0.97054	0.971137	0.000597
-1	-1	0.8	0.01	0.83037	0.829712	0.000658
0.5	-0.3	1	0.1	0.90166	0.902353	0.000693
1	-0.3	0.8	0.01	0.95488	0.954177	0.000703
0.5	0.3	1	0.08	0.95857	0.957817	0.000753
-0.3	-0.3	1	0.08	0.88279	0.883552	0.000762
-1	0	0.8	0.04	0.89277	0.891859	0.000911

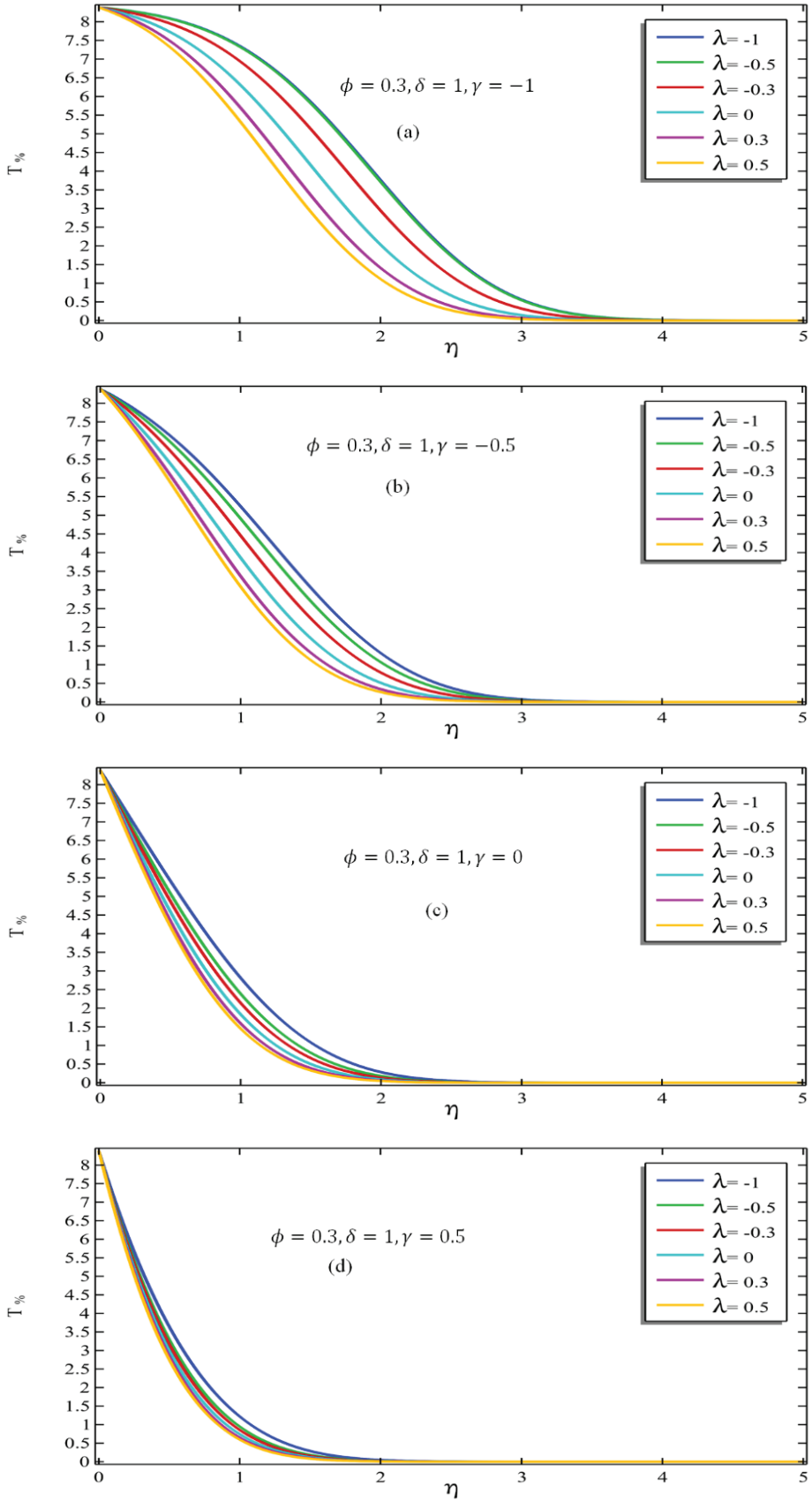

Figure 7. (a-d) Temperature distribution against the increasing value of η for all values of λ and suction/injection parameter with fixed δ and volume fraction of nanofluids.

Pattern of Percentage Change Due To Ambient Temperature

In this section, we will discuss temperature distribution patterns. As you may recall, in the similarity transformation, we transformed the temperature variable T into the similarity variable θ, as shown in equation (6). Now, we are analyzing the same equation for a particular case. We are discussing a specific case where T_w = 323.15, representing the wall temperature, and T_∞ = 293.25, representing the ambient temperature. Our objective here is to analyze the pattern by altering selected non-dimensional parameters such as λ, δ, ϕ, and γ. The formula to calculate $T_{\%}$ is given as under:

$$T_{\%} = 100\left(\frac{T - T_\infty}{T_\infty}\right) \tag{18}$$

We have produced Figure 7(a-d), which shows the percentage change due to ambient temperature as a function of η. In these figures, ϕ and δ values are fixed while λ and γ values are altered. In Figure 7(a), we can observe a negative relationship between $T_{\%}$ and η for almost all the graphs. This means that as we increase η values, $T_{\%}$ decreases. We can see that for all fixed parameter values, the temperature percentage is decreasing. In Figure 7(a), we can see that as we increase λ values from -1 to 0.5, the temperature percentage decrement becomes faster. It's worth noting that an injection condition is applied here because γ = -1. In Figure

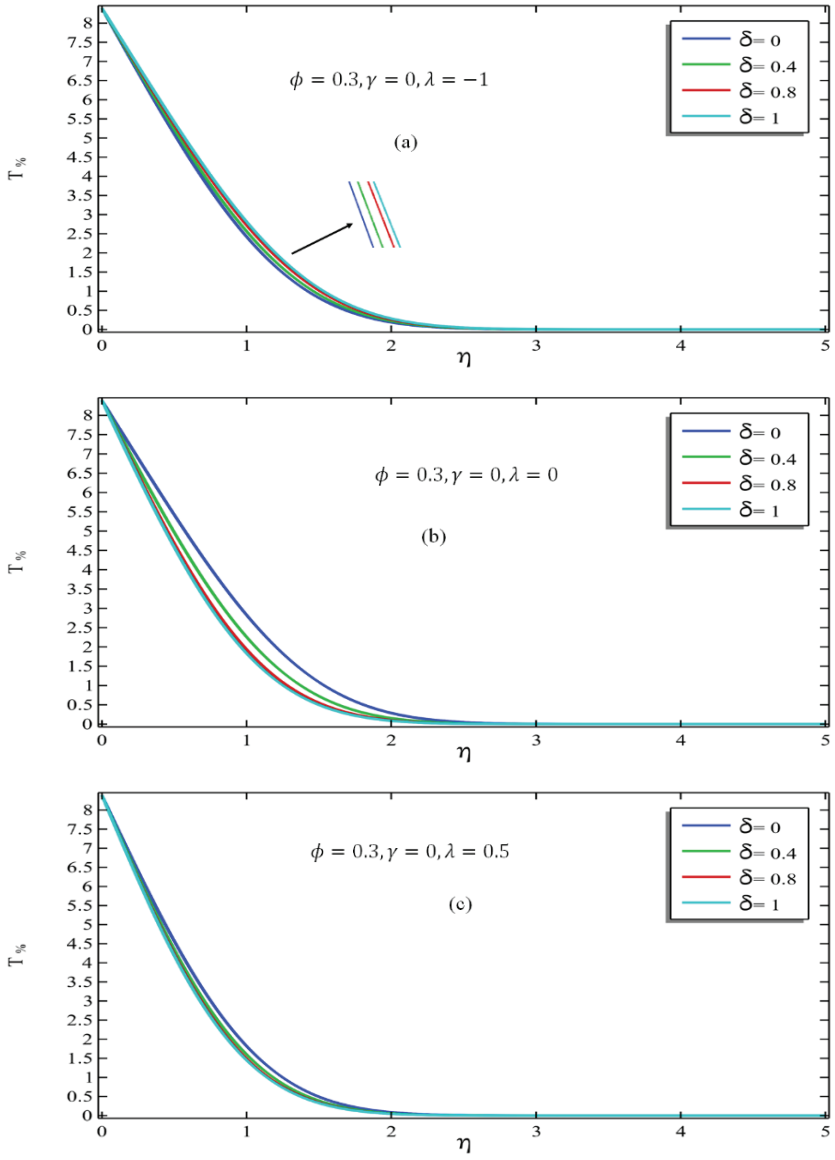

Figure 8. (a-d) Temperature distribution vs η for all the values of δ and λ values with fixed γ values and volume fraction of nanofluids.

7(b), we set γ = -0.5 and reduced the injection condition. You can see that $T_{\%}$ is constantly decreasing for all fixed λ values, but the width between the graphs, which represents the impact of reducing the injection condition, has also decreased. This means that the difference in the rate of decrement for different λ values has reduced. This can be observed in Figure 7(c).

Here, we set γ = 0, which means there is no suction or injection. We can see that as we increase λ values, $T_{\%}$ decreases rapidly. Additionally, the difference in $T_{\%}$ due to λ values has also reduced compared to previous cases. Finally, in Figure 7(d), we set γ = 0.5, and it can be observed that increasing λ values result in a significant decrease in heat transfer rate compared to ambient temperature.

In Figure 8(a-c), we maintained a constant volume fraction of nanofluids and the absence of suction/injection while adjusting the values of λ and the slip flow parameter to observe the percentage change in temperature due to ambient temperature. In Figure 8(a), as the slip flow parameter δ increases from 0 to 1, there is a noticeable decrease in the percentage change in temperature due to ambient temperature. Similarly, in Figure 8(b), with all other parameters identical to those in Figure 8(a) except for λ, set to zero to indicate a horizontally stationary sheet, increasing the slip flow parameter results in a reduction in $T_{\%}$ declination. This contrasts with the scenario in Figure 8(a), where declination implies that, for the same value of η, $T_{\%}$ diminishes with increasing δ values. Proceeding to Figure 8(c), it's essential to highlight that positive values of λ denote a stretching sheet. Here, it is evident that for the same value of η, $T_{\%}$ increases with a rising value of the slip flow parameter. This pattern differs significantly from what we observed in Figure 8(a).

In Figure 9(a-d), we have presented numerical results to observe variations. Here, we set γ and λ to zero, indicating no suction or injection, and the sheet is stationary. We are examining the value of $T_{\%}$ with changes in ϕ and δ, representing a percentage change due to ambient temperature. In Figure 9(a), it is evident that as the values of ϕ increase, $T_{\%}$ also increases for the same value of η. This implies that the original temperature T is rising compared to the ambient temperature T_{∞} as the volume fraction of water-based nanofluids increases. This characteristic of ternary nanofluids, observed for a decade, indicates their enhanced effectiveness in increasing the heat transfer rate compared to conventional fluids. Next, let's consider Figure 9(b-d), where we observe δ values from 0.4 to 1. It is clear that increasing the volume fraction of ternary nanofluids results in an increment in the heat transfer rate from all aspects. Here, γ and λ are zero, signifying no suction or injection, and the sheet is stationary. If we include them, they would contribute to heat transfer in a similar manner as discussed earlier.

Physical mechanism

The elucidation of numerical results reveals an intriguing and noteworthy physical mechanism. Notably, the increase in the volume fraction of nanomaterials within the base fluids does not act as a coolant. Instead, it contributes to heightened temperatures from the wall to the surrounding environment, attributed to the increased thermal conductivity within the domain. Furthermore, the observation that a shrinking sheet supports temperature enhancement is noteworthy. This enhancement occurs due to its virtue of collecting a greater volume of fluid at a single point. The application or augmentation of the suction effect further facilitates fluid drainage from the sheet, resulting in a decrease in fluid volume and subsequently lowering the temperature. Consequently, an enhancement in suction parameters leads to a decrease in temperature. Additionally, permitting more slip flow conditions increases fluid velocity, causing a larger quantity to drain out through the outlet or suction effects, ultimately resulting in a decline in temperature. In conclusion, the manipulation of various parameters provides a means to control temperature effectively.

Implementing an online calculator [65-67], we used statistical tools to estimate the regression equation or the best-fit equation relating to the four parameters in the present study. This equation is presented as (19). To validate this equation, we have also included Table 6, which displays the top 20 parameters that yield the minimum error when comparing the average temperature profile with the one calculated from the regression equation. From Table 5, it can be understood that using the values of γ = 0.5, λ = 0, δ = 1 and ϕ_3 = 0.04, the equation (19) can work better as the estimator for average temperature profile.

$$\hat{\theta(\eta)}_{avg} = 0.116019 - 0.131626\gamma - 0.0326314\lambda - 0.0171223\delta + 0.521582\phi_3 \quad (19)$$

Pattern of Nusselt Number Against Altering the Parameters

In this section, we have dedicated our focus to scrutinizing the Nusselt number's behavior in response to varying λ values. The Nusselt number, as commonly understood, represents the ratio between convection and conduction phenomena. A pivotal insight to consider is that an elevation in the Nusselt number accentuates stronger convection, while a reduction favors more pronounced conduction processes. In Figure 10(a-d), we present a series of plots illustrating the Nusselt number's dependency on λ values, maintaining a constant volume fraction set at 0.3. In Figure 10(a), where γ = -1 (injection case), a noteworthy trend is observed. Specifically, when δ is 0, the Nusselt number exhibits a decrement as λ values progress from -1 to 0, followed by an increment after λ reaches 0. Each graph in Figure 10(a), corresponding to fixed δ values, displays an initial reduction in the Nusselt number until a critical value of λ is reached, beyond which an increase is observed.

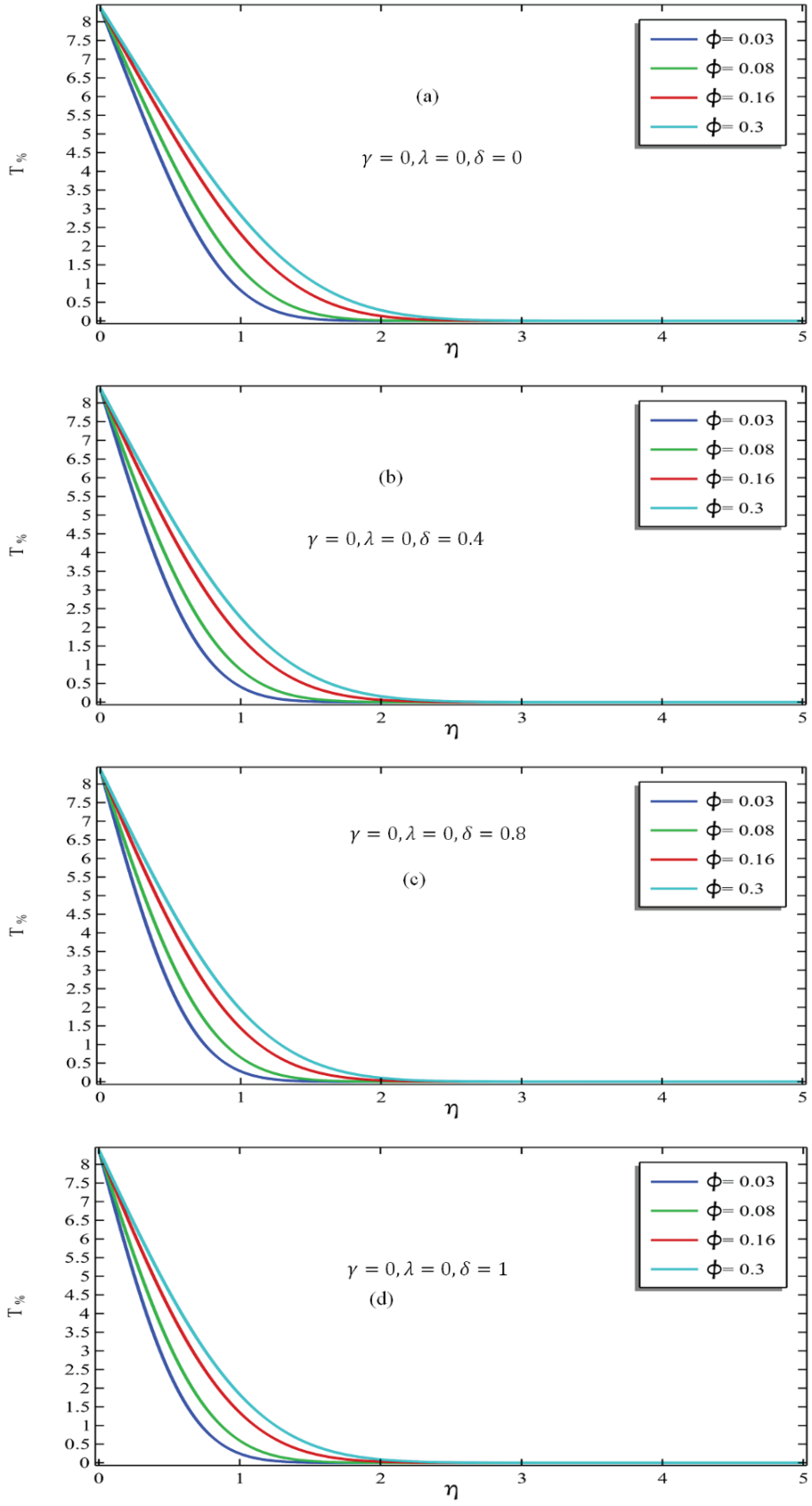

Figure 9. (a-d) Temperature distribution vs η for all the volume fraction of nanofluids and slip flow parameters with fixed values of γ and λ values.

Table 6. Top 20 values of the parameters that yield the minimum error when comparing the average temperature profile with the one calculated from the regression equation

γ	λ	δ	ϕ_3	$\theta(\eta)_{avg}$	$\hat{\theta(\eta)}_{avg}$	$\lvert \theta(\eta)_{avg} - \hat{\theta(\eta)}_{avg} \rvert$
0.5	0	1	0.04	0.053949	0.053947	2.02E-06
-1	0.5	0.8	0.04	0.23854	0.238495	4.53E-05
0.5	0.3	0.4	0.04	0.054485	0.054431	5.41E-05
0.5	0	0.4	0.1	0.095422	0.095515	9.33E-05
-1	0.3	0.8	0.1	0.27601	0.276316	0.000306
0.3	0.5	1	0.1	0.094897	0.095251	0.000354
-1	0.5	1	0.04	0.23466	0.23507	0.00041
0.5	0	0.8	0.01	0.042154	0.041724	0.00043
0.3	0.5	1	0.01	0.048761	0.048309	0.000452
0.5	0.3	0.4	0.08	0.075776	0.075294	0.000482
0.5	0	1	0.08	0.075312	0.07481	0.000502
-0.5	-1	0.8	0.04	0.22077	0.221629	0.000859
-1	0.3	1	0.08	0.26106	0.26246	0.0014
-1	0.3	0.8	0.08	0.26729	0.265884	0.001406
-0.5	-0.3	0.8	0.1	0.23155	0.230082	0.001468
-0.5	-0.5	1	0.08	0.22122	0.222752	0.001532
0.5	0	0.8	0.08	0.07656	0.078235	0.001675
0.5	0	0.8	0.1	0.090431	0.088666	0.001765
0.5	-0.3	0.4	0.1	0.10341	0.105305	0.001895
-0.5	0	0.4	0.1	0.22523	0.227141	0.001911

Notably, this analysis focuses on a unique scenario where δ = 1, revealing a distinctive surge in the Nusselt number at a critical λ value.

Similarly, in Figure 10(b) with γ = -0.5 (injection case), a parallel observation emerges. The Nusselt number initially diminishes with increasing λ values, followed by a subsequent increase beyond a critical λ value, except in cases where δ = 1. Extending this analysis to Figure 10(c) and Figure 10(d), representing no injection and suction cases, respectively, reveals consistent patterns. For scenarios where δ assumes values of 0 and 0.4, the Nusselt number experiences a decline until reaching a critical λ value, after which a discernible increase is noted. The conclusive finding is that the Nusselt number undergoes a significant increment only when δ assumes values of 0.8 and 1. This signifies a crucial enhancement in the Nusselt number under these specific conditions.

In Figure 11(a-d), we systematically examined the Nusselt number, maintaining a constant ϕ value for each curve while setting δ = 1 across all graphs. Within Figure 11(a), delineating an injection scenario with a fixed γ = -1, a discernible trend emerged. For each fixed ϕ value, the Nusselt number exhibited an increase as the λ value ascended from -1 to 0.5. This trend denotes an augmented convection process concomitant with the rise in the volume fraction of ternary nanofluids. Notably, Figure 11(a) showcased a critical λ value for each volume fraction, triggering an accelerated convection process.

Transitioning to Figure 11(b) and Figure 11(c), portraying injection and no injection/suction cases, respectively, a similar pattern persisted. As λ values increased for each fixed ϕ, the Nusselt number demonstrated a consistent ascent. In Figure 11(d), under the suction condition with a fixed γ = 0.5, an intriguing dynamic unfolded. Elevating λ values corresponded to an increase in the Nusselt number, while a concurrent rise in the volume fraction ϕ resulted in a decline in the Nusselt number. This observed behavior presented a distinctive contrast to the scenarios studied in Figure 11(a-c).

Physical mechanism

Our observations revealed that when dealing with a shrinking sheet, the Nusselt number increased. This suggests that the conduction process became more dominant compared to convection. When we increased the slip effect, which means more fluid is draining out through suction, the convection process strengthened. Additionally, as we increased the volume fraction of nanomaterials, the convection process improved, allowing for more efficient heat transfer from the surroundings to the fluids. Consequently, in our results, we found that the Nusselt number increased due to the higher volume fraction.

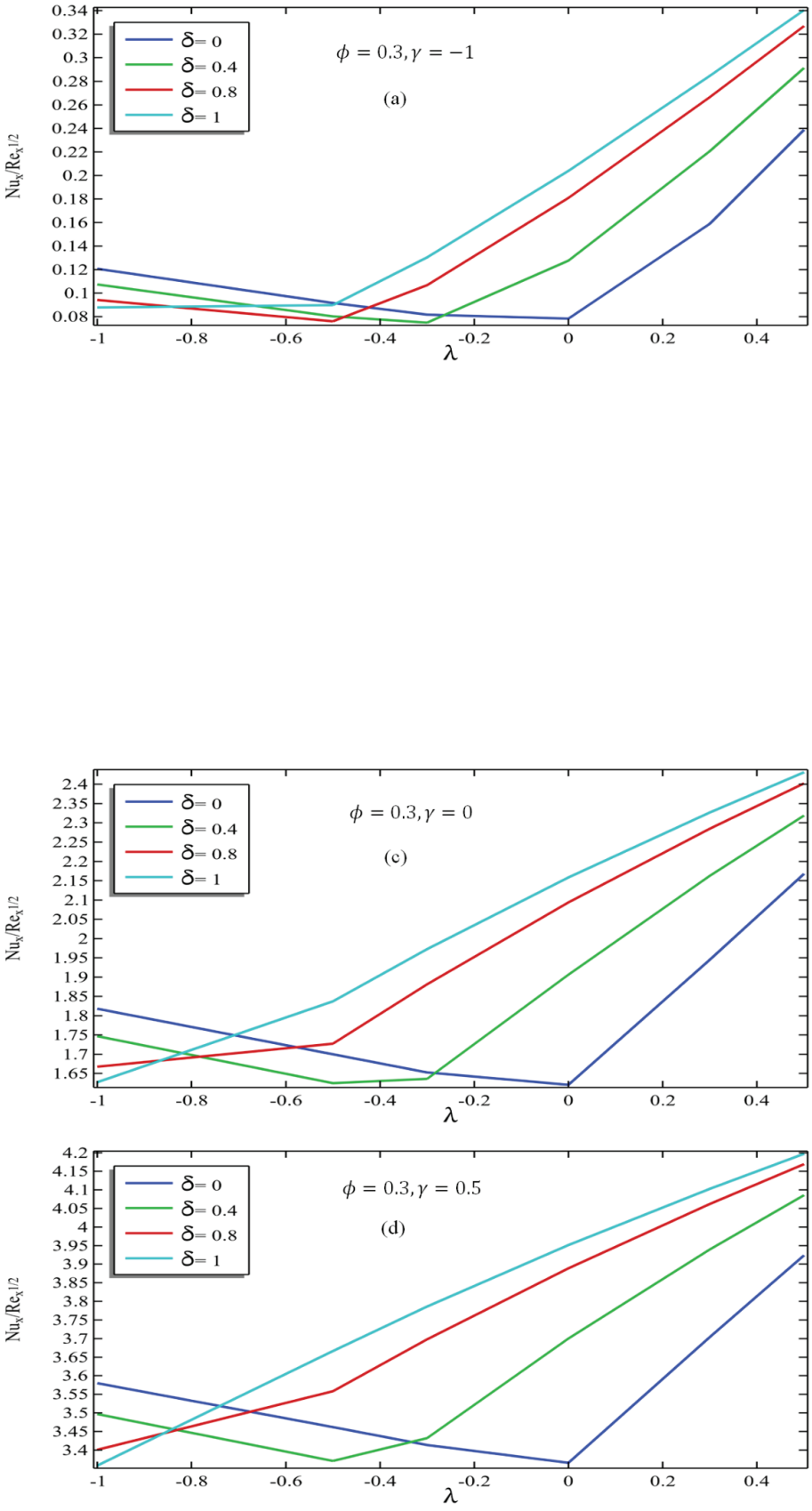

Figure 10. (a-d) Local Nusselt number vs the λ values for all slip flow parameters and suction/injection parameters with fixed volume fraction of nanofluids.

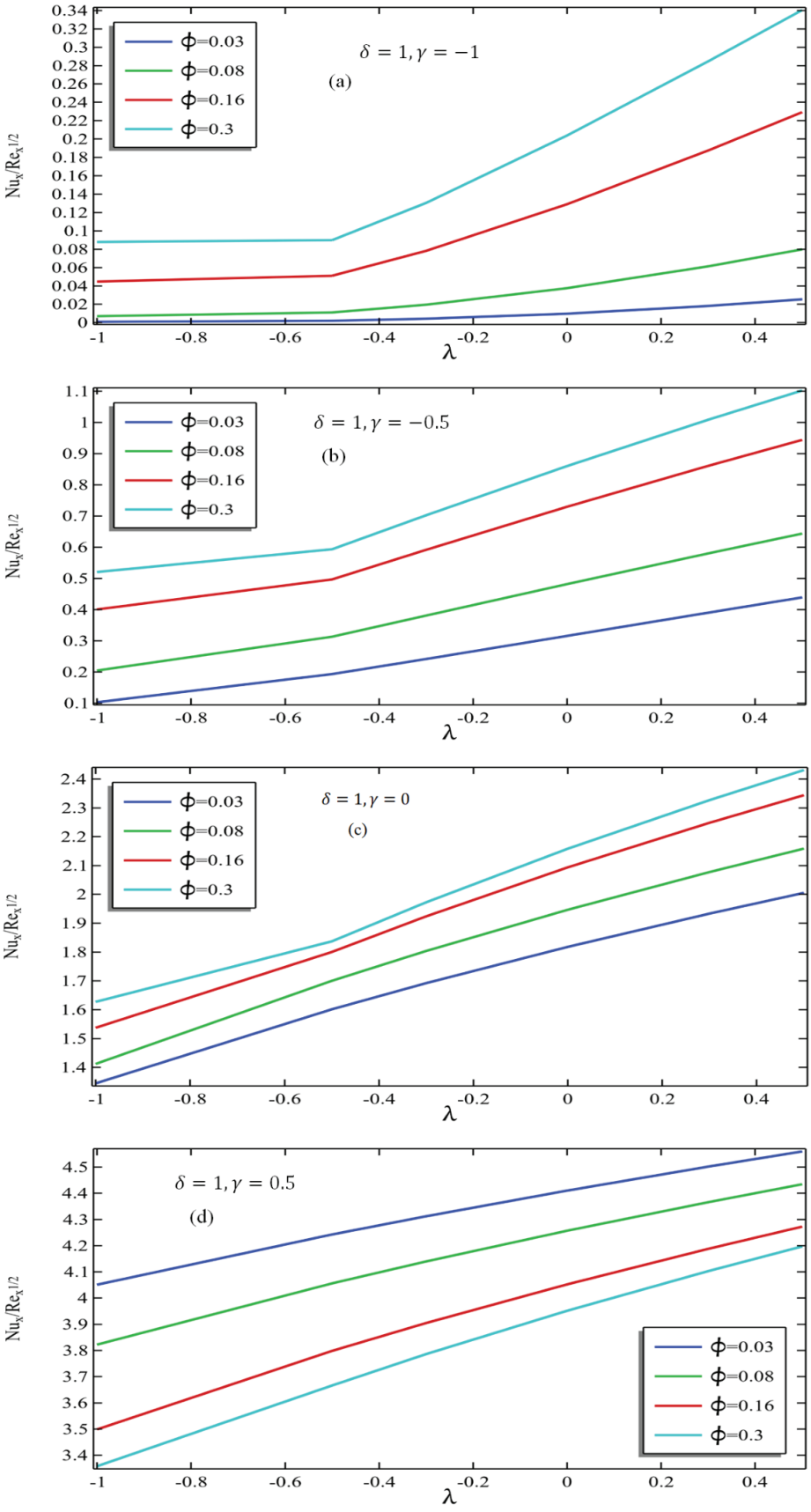

Figure 11. (a-d) Local Nusselt number vs the λ values for all γ values and volume fraction with fixed slip flow parameters.

CONCLUSION

In this study, we delved into the stagnation point flow scenarios involving a stretching and shrinking sheet, exploring the dynamic and thermal characteristics of ternary-based nanofluids comprised of titanium oxide, silver, and zinc oxide. Leveraging the finite element package COMSOL Multiphysics and adopting the Tiwari and Das model for boundary layer flow, we converted governing boundary flow equations into ordinary differential equations (ODEs) and implemented them within the mathematics interface of the FEM package. The investigation spanned various key variables, such as velocity profile, temperature distribution for a specific case, and Nusselt number, with a focus on varying parameters including slip flow, suction/injection, stretching/shrinking, and volume fraction of nanofluids. The primary conclusions can be summarized as follows:

- Across fixed parameter values, the velocity profile exhibited an increase with rising η. Moreover, maintaining a constant volume fraction and slip flow parameter revealed an improved velocity profile with increasing λ values from -1 to 0.5 in cases of suction or injection.
- Sheet stretching, with increasing δ values, resulted in a decrease in the velocity profile. Conversely, for a stationary or stretching sheet, increasing δ values projected an increase in the velocity profile. This observation remained consistent when the volume fraction was fixed, and there was no suction or injection involved.
- In scenarios with a stationary sheet and no suction or injection, an increase in the volume fraction led to a decrease in the velocity field. Meanwhile, increasing δ values amplified the velocity profile, while other alterations in the volume fraction had an insignificant impact.
- The percentage change due to ambient temperature consistently decreased with increasing η, whether the sheet was stretching or shrinking. The temperature decline was more rapid in the case of a shrinking sheet. In injection cases, alterations in λ values had a more significant impact on the percentage change in temperature compared to suction cases.
- In cases involving the volume fraction of nanofluids and the absence of suction/injection during shrinking, increasing the slip flow parameter led to a decrease in the heat transfer rate. Conversely, for a stretching or stationary sheet, increasing the slip flow parameter led to an increase in the heat transfer rate for the same values of η.
- When the sheet was stationary and devoid of suction or injection, an increase in the volume fraction of nanofluids resulted in an increase in the heat transfer rate, indicating a rise in temperature compared to the ambient temperature. However, when the slip flow parameter was increased within this range, the heat transfer rate due to ambient temperature decreased, albeit insignificantly.
- In injection cases, increasing λ values initially led to a decrease in the Nusselt number for each value of δ from 0 to 0.8. However, after reaching a critical value of λ, the Nusselt number began to increase. Additionally, in cases with no suction or suction, the Nusselt number increased only when δ had values of 0.8 and 1, indicative of a stronger convection process.
- The study concluded that increasing λ values and the volume fraction of ternary nanofluids in either suction or injection cases yielded a positive response in the Nusselt number. However, when considering the suction case alone, although the Nusselt number increased with increasing λ values from -1 to 0.5, it decreased with an increase in the volume fraction of nanofluids.

In conclusion, our research provides important new understandings of the complex dynamics of stagnation point flow and ternary nanofluid thermal behavior. The practical implications of these findings are noteworthy as they provide insights into possible improvements in heat transfer procedures and direct future research efforts in the field of nanofluid-based technology.

Future Direction: This study delves into the exploration of stagnation point flow in the context of stretching and shrinking phenomena, incorporating suction/injection and accounting for slip flow parameters. The chosen passage fluids through the sheet are ternary nanofluids, and their thermophysical properties are derived using a simplified model. The investigation involves varying parameters to elucidate the results concerning velocity profiles, percentage changes in temperature, and Nusselt numbers. The discourse on results has yielded valuable insights.

Moving forward, the same formulation can be seamlessly applied to extend the inquiry into fluid flow and heat transfer using the bi-quadratic hybrid model of nanofluids, permitting the exploration of a wider range of parameter values. Additionally, the robustness of the results presented here is affirmed through verification against numerical solutions derived from the governing equations transformed through the similarity process. This opens avenues for further exploration and validation, contributing to the broader understanding of stagnation point flow dynamics and its applications.

AUTHORSHIP CONTRIBUTIONS

Authors equally contributed to this work.

DATA AVAILABILITY STATEMENT

The authors confirm that the data that supports the findings of this study are available within the article. Raw data that support the finding of this study are available from the corresponding author, upon reasonable request.

CONFLICT OF INTEREST

The author declared no potential conflicts of interest with respect to the research, authorship, and/or publication of this article.

ETHICS

There are no ethical issues with the publication of this manuscript.

REFERENCES

[1] Hiemenz K. Die Grenzschicht an einem in den gleichformigen Flussigkeitsstrom eingetauchten geraden Kreiszylinder. Dinglers Polytech J 1911;326:321−324. [German]

[2] Homann F. Der Einfluss grosser Zähigkeit bei der Strömung um den Zylinder und um die Kugel. J Appl Math Mech (ZAMM) 1936;16:153−164. [German] [CrossRef]

[3] Chiam TC. Stagnation-point flow towards a stretching plate. J Physic Soc Japan 1994;63:2443−2444. [CrossRef]

[4] Khashi'ie NS, Arifin NM, Rashidi MM, Hafidzuddin EH, Wahi N. Magnetohydrodynamics (MHD) stagnation point flow past a shrinking/stretching surface with double stratification effect in a porous medium. J Therm Anal Calorim 2020;139:3635−3648. [CrossRef]

[5] Choi SUS, Eastman JA. Enhancing thermal conductivity of fluids with nanoparticles (No. ANL/MSD/CP-84938; CONF-951135-29). ASME International Mechanical Engineering Congress & Exposition, November 12-17, 1995, San Francisco.

[6] Lee S, Choi SUS, Li S, Eastman JA. Measuring thermal conductivity of fluids containing oxide nanoparticles. J Heat Transf 1999;121:280−289. [CrossRef]

[7] Keblinski P, Phillpot SR, Choi SUS, Eastman JA. Mechanisms of heat flow in suspensions of nano-sized particles (nanofluids). Int J Heat Mass Transf 2002;45:855−863. [CrossRef]

[8] Kumar MD, Raju CSK, Sajjan K, El-Zahar ER, Shah NA. Linear and quadratic convection on 3D flow with transpiration and hybrid nanoparticles. Int Comm Heat Mass Transf 2022;134:105995. [CrossRef]

[9] Upadhya SM, Raju SSR, Raju CSK, Shah NA, Chung JD. Importance of entropy generation on casson, micropolar and hybrid magneto-nanofluids in a suspension of cross diffusion. Chinese J Physics 2022;77:1080−1101. [CrossRef]

[10] Al-Kouz W, Abderrahmane A, Shamshuddin MD, Younis O, Mohammed S, Bég OA, et al. Heat transfer and entropy generation analysis of water-Fe3O4/CNT hybrid magnetic nanofluid flow in a trapezoidal wavy enclosure containing porous media with the Galerkin finite element method. Eur Physic J Plus 2021;136:1184. [CrossRef]

[11] Bin Mizan MR, Ferdows M, Shamshuddin MD, Bég OA, Salawu SO, Kadir A. Computation of ferromagnetic/nonmagnetic nanofluid flow over a stretching cylinder with induction and curvature effects. Heat Transf 2021;50:5240−5266. [CrossRef]

[12] Rahman M, Ferdows M, Shamshuddin MD, Koulali A, Eid MR. Aiding (opponent) flow of hybrid copper-aluminum oxide nanofluid towards an exponentially extending (lessening) sheet with thermal radiation and heat source (sink) impact. J Petrol Sci Engineer 2022;215:110649. [CrossRef]

[13] Salawu SO, Shamshuddin MD, Beg OA. Influence of magnetization, variable viscosity and thermal conductivity on Von Karman swirling flow of H2O-FE3O4 and H2O-Mn-ZNFe2O4 ferromagnetic nanofluids from a spinning DISK: Smart spin coating simulation. Mater Sci Engineer B 2022;279:115659. [CrossRef]

[14] Buongiorno J. Convective transport in nanofluids. J Heat Transf 2006;128:240−250. [CrossRef]

[15] Tiwari RK, Das MK. Heat transfer augmentation in a two-sided lid-driven differentially heated square cavity utilizing nanofluids. Int J Heat Mass Transf 2007;50:2002−2018. [CrossRef]

[16] Reza-E-Rabbi S, Ahmmed SF, Arifuzzaman SM, Sarkar T, Khan MS. Computational modelling of multiphase fluid flow behaviour over a stretching sheet in the presence of nanoparticles. Engineer Sci Technol 2020;23:605−617. [CrossRef]

[17] Rana BMJ, Arifuzzaman SM, Reza-E-Rabbi S, Ahmed SF, Khan MS. Energy and magnetic flow analysis of Williamson micropolar nanofluid through stretching sheet. Int J Heat Technol 2019;37:487−496. [CrossRef]

[18] Vijatha M. Reddy PBA. Comparative analysis on magnetohydrodynamic flow of non-Newtonian hybrid nanofluid over a stretching cylinder: Entropy generation. J Process Mech Engineer 2022;236:2361−2371. [CrossRef]

[19] Nield DA, Kuznetsov AV. The Cheng-Minkowycz problem for natural convective boundary-layer flow in a porous medium saturated by a nanofluid. Int J Heat Mass Transf 2009;52:5792−5795. [CrossRef]

[20] Nield DA, Kuznetsov AV. The Cheng-Minkowycz problem for the double-diffusive natural convective boundary layer flow in a porous medium saturated by a nanofluid. Int J Heat Mass Transf 2011;54:374−378. [CrossRef]

[21] Kuznetsov AV, Nield DA. Natural convective boundary-layer flow of a nanofluid past a vertical plate. Int J Therm Sci 2010;49:243−247. [CrossRef]

[22] Kuznetsov AV, Nield DA. Double-diffusive natural convective boundary-layer flow of a nanofluid past a vertical plate. Int J Therm Sci 2011;50:712−717. [CrossRef]

[23] Bachok N, Ishak A, Pop I. Boundary-layer flow of nanofluids over a moving surface in a flowing fluid. Int J Therm Sci 2010;49:1663−1668. [CrossRef]
[24] Bachok N, Ishak A, Pop I. Unsteady boundary-layer flow and heat transfer of a nanofluid over a permeable stretching/shrinking sheet. Int J Heat Mass Transf 2012;55:2102−2109. [CrossRef]
[25] Khan WA, Aziz A. Natural convection flow of a nanofluid over a vertical plate with uniform surface heat flux. Int J Therm Sci 2011;50:1207−1214. [CrossRef]
[26] Ferdows M, Shamshuddin MD, Salawu SO, Sun S. Thermal cooling performance of convective non-Newtonian nanofluid flowing with variant power-index across moving extending surface. Sci Rep 2022;12:8714. [CrossRef]
[27] Devi SA, Devi SSU. Numerical investigation of hydromagnetic hybrid Cu-Al2O3/water nanofluid flow over a permeable stretching sheet with suction. Int J Nonlinear Sci Numer Sim 2016;17:249−257. [CrossRef]
[28] Rohsenow WM, Hartnett JP, Ganic EN. Handbook of Heat Transfer Fundamentals. New York: McGraw-Hill; 1985.
[29] Masad JA, Nayfeh AH. Effects of suction and wall shaping on the fundamental parametric resonance in boundary layers. Physics Fluids A 1992;4:963−974. [CrossRef]
[30] Rosali H, Ishak A, Pop I. Micropolar fluid flow towards a stretching/shrinking sheet in a porous medium with suction. Int Comm Heat Mass Transf 2012;39:826−829. [CrossRef]
[31] Crane LJ. Flow past a stretching plate. J Appl Math Physics (ZAMP) 1970;21:645−647. [CrossRef]
[32] Bakr SA, Thumma T, Ahmed SE, Mansour MA, Morsy Z. Effects of wavy porous fins on the flow, thermal fields, and entropy of the magnetic radiative non-Newtonian nanofluid confined inclined enclosures. J Proc Mech Engineer 2022;09544089211072629. [RETRACTED] [CrossRef]
[33] Dawar A, Wakif A, Thumma T, Shah NA. Towards a new MHD non-homogeneous convective nanofluid flow model for simulating a rotating inclined thin layer of sodium alginate-based Iron oxide exposed to incident solar energy. Int Comm Heat Mass Transf 2022;130:105800. [CrossRef]
[34] Thumma T, Bég OA, Kadir A. Numerical study of heat source/sink effects on dissipative magnetic nanofluid flow from a non-linear inclined stretching/shrinking sheet. J Molecular Liquid 2017;232:159−173. [CrossRef]
[35] Thumma T, Mishra SR, Abbas MA, Bhatti MM, Abdelsalam SI. Three-dimensional nanofluid stirring with non-uniform heat source/sink through an elongated sheet. Appl Math Comp 2022;421:126927. [CrossRef]
[36] Boroomandpour A, Toghraie D, Hashemian M. A comprehensive experimental investigation of thermal conductivity of a ternary hybrid nanofluid containing MWCNTs-titania-zinc oxide/water-ethylene glycol (80: 20) as well as binary and mono nanofluids. Synthetic Metals 2020;268:116501. [CrossRef]
[37] Dezfulizadeh A, Aghaei A, Joshaghani AH, Najafizadeh MM. An experimental study on dynamic viscosity and thermal conductivity of water-Cu-SiO2-MWCNT ternary hybrid nanofluid and the development of practical correlations. Powder Technol 2021;389:215−234. [CrossRef]
[38] Mohammadfam Y, Heris SZ. Thermophysical characteristics and forced convective heat transfer of ternary doped magnetic nanofluids in a circular tube: An experimental study. Case Stud Therm Engineer 2023;52;103748. [CrossRef]
[39] Usharani P, Ravindra Reddy B. Thermodynamic analysis of EMHD ternary nanofluid flow with shape factor effects over a shrinking sheet: A non-Fourier heat flux model. Numer Heat Transf Part A Appl 2024;1−24. [CrossRef]
[40] Goyal K, Srinivas S. Pulsatile flow of Casson hybrid nanofluid between ternary-hybrid nanofluid and nanofluid in an inclined channel with temperature-dependent viscosity. Numer Heat Transf Part A Appl 2024;1−30. [CrossRef]
[41] Uddin MJ, Amirsom NA, Bég OA, Ismail AI. Computation of bio-nano-convection power law slip flow from a needle with blowing effects in a porous medium. Waves in Random and Complex Media, 2022;1−21. [CrossRef]
[42] Bég OA, Uddin MJ, Bég TA, Kadir A, Shamshuddin MD, Babaie M. Numerical study of self-similar natural convection mass transfer from a rotating cone in anisotropic porous media with Stefan blowing and Navier slip. Indian J Physic 2020;94:863−877. [CrossRef]
[43] Beg OA, Zohra FT, Uddin MJ, Ismail AIM, Sathasivam S. Energy conservation of nanofluids from a biomagnetic needle in the presence of Stefan blowing: Lie symmetry and numerical simulation. Case Stud Therm Engineer 2021;24:100861. [CrossRef]
[44] Maxwell JC. VII. On stresses in rarified gases arising from inequalities of temperature. Phil Trans R Soc 1879;170:231−256. [CrossRef]
[45] Wang CY. Stagnation flows with slip: exact solutions of the Navier-Stokes equations. J Appl Math Physics (ZAMP) 2003;1:184−189. [CrossRef]
[46] Paul A, Patgiri B, Sarma N. Darcy-Forchheimer flow of Ag-ZnO-CoFe2O4/H2O Casson ternary hybrid nanofluid induced by a rotatory disk with EMHD. Int J Amb Energy 2024;45:2313697. [CrossRef]
[47] Paul A, Patgiri B, Sarma N. Transformer oil-based Casson ternary hybrid nanofluid flow configured by a porous rotating disk with hall current. J Appl Math Mech (ZAMM) 2024:104:202300704. [CrossRef]

[48] Paul A, Sarma N, Patgiri B. Numerical assessment of MHD thermo-mass flow of casson ternary hybrid nanofluid around an exponentially stretching cylinder. BioNanoScience 2024;1−16. [CrossRef]
[49] Khan U, Ahmed N, Asadullah M, Mohyud-din ST. Effects of viscous dissipation and slip velocity on two-dimensional and axisymmetric squeezing flow of Cu-water and Cu-kerosene nanofluids. Propul Power Res 2015;4:40−49. [CrossRef]
[50] Bég OA, Kabir MN, Uddin MJ, Izani Md Ismail A, Alginahi YM. Numerical investigation of Von Karman swirling bioconvective nanofluid transport from a rotating disk in a porous medium with Stefan blowing and anisotropic slip effects. J Mech Engineer Sci 2021;235:3933−3951. [CrossRef]
[51] Latiff NA, Uddin MJ, Ismail AM. Stefan blowing effect on bioconvective flow of nanofluid over a solid rotating stretchable disk. Propul Power Res 2016;5:267−278. [CrossRef]
[52] Tuz Zohra F, Uddin MJ, Basir MF, Ismail AIM. Magnetohydrodynamic bio-nano-convective slip flow with Stefan blowing effects over a rotating disc. J Nanomater Nanoengineer Nanosys 2020;234:83−97. [CrossRef]
[53] Uddin MJ, Kabir MN, Alginahi Y, Bég OA. Numerical solution of bio-nano convection transport from a horizontal plate with blowing and multiple slip effects. J Mech Engineer Sci 2019;233:6910−6927. [CrossRef]
[54] Elhag SH, Memon AA, Memon MA, Bhatti K, Jacob K, Alzahrani S, et al. Analysis of forced convection with hybrid Cu-Al2O3 nanofluids injected in a three-dimensional rectangular channel containing three perpendicular rotating blocks with turbulent modeling. J Nanomater 2022;2:1−27. [CrossRef]
[55] Memon AA, Khan WA, Muhammad T. Numerical investigation of photovoltaic thermal energy efficiency improvement using the backward step containing Cu-Al2O3 hybrid nanofluid. Alexandria Engineer J 2023;75:391−406. [CrossRef]
[56] Alghamdi M, Memon AA, Muhammad T, Ali M. A numerical investigation of a photovoltaic thermal system contained a trapezoidal channel with transport of silver and titanium oxide using the water as base fluids. Case Stud Therm Engineer 2023;47:103056. [CrossRef]
[57] Alqarni MM, Memon AA, Memon MA, Mahmoud EE, Fenta A. Numerical investigation of heat transfer and fluid flow characteristics of ternary nanofluids through convergent and divergent channels. Nanoscale Advances 2023;5:6897−6912. [CrossRef]
[58] Allehiany FM, Memon AA, Memon MA, Fenta A. Maximizing electrical output and reducing heat-related losses in photovoltaic thermal systems with a thorough examination of flow channel integration and nanofluid cooling. Sci Rep 2023;13:16961. [CrossRef]
[59] Akram M, Memon AA, Memon MA, Obalalu AM, Khan U. Investigation of a two-dimensional photovoltaic thermal system using hybrid nanofluids and a rotating cylinder. Nanoscale Advances 2023;5:5529−5542. [CrossRef]
[60] Memon AA, Memon MA, Haque MM. Numerical investigation of electrical efficiency with the application of hybrid nanofluids for photovoltaic thermal systems contained in a cavity channel. J Math 2023:1−18. [CrossRef]
[61] Yashkun U, Zaimi K, Bakar NAA, Ferdows M. Nanofluid stagnation-point flow using Tiwari and Das model over a stretching/shrinking sheet with suction and slip effects. J Adv Res Fluid Mech Therm Sci 2020;70:62−76. [CrossRef]
[62] Mahmood Z, Alhazmi SE, Alhowaity A, Marzouki R, Al-Ansari N, Khan U. MHD mixed convective stagnation point flow of nanofluid past a permeable stretching sheet with nanoparticles aggregation and thermal stratification. Sci Rep 2022;12:16020. [CrossRef]
[63] Jawad M, Khan Z, Bonyah E, Jan R. Analysis of hybrid nanofluid stagnation point flow over a stretching surface with melting heat transfer. Mathl Problems Engineer 2022:1−12. [CrossRef]
[64] Nadeem S, Khan MR, Khan AU. MHD stagnation point flow of viscous nanofluid over a curved surface. Physica Scripta 2019;94:115207. [CrossRef]
[65] Datta A, Halder P. Field-synergy and nanoparticle's diameter analysis on circular jet impingement using three oxide-water-based nanofluids. J Therm Engineer 2023;9:179−190. [CrossRef]
[66] Babu MS, Ramana VV, Shankar GR, Raju C. Mixed convective flow of heat and mass transfer of nanofluids over a static wedge with convective boundary conditions. J Therm Engineer 2021;8;1958-1969. [CrossRef]
[67] Estellé P, Halelfadl S, Maré T. Thermal conductivity of CNT water based nanofluids: Experimental trends and models overview. J Therm Engineer 2015;1:381−390. [CrossRef]